

# Electrolytes and Cathode Designs for Next Generation of Silicon-based Batteries – Comprehensive Experimental and Computational Considerations

Alon Epshtain,<sup>[a]</sup> Igor Baskin,<sup>[a]</sup> and Yair Ein-Eli<sup>\*[a, b]</sup>

The increasing demand for energy storage technologies has prompted the exploration of side-by-side technologies, that can complement the current Lithium-ion battery industry with cheaper and more abundant materials that can be incorporated in a myriad of new electrochemical cell designs. To meet these goals, a novel approach for electrolyte design using quantum-mechanical density function theory (DFT) modeling was implemented in concert with experimental electrochemical characterization to culminate in a predictive model that can be tailored to a specific cell chemistry. Physical characteristics as dielectric constant, solvent acidity, basicity etc. influence fluoride speciation, solvation and electrolyte performance, in an

iterative fashion to enable characterization prediction of <sup>19</sup>F NMR shifts, ionic conductivity mechanisms and fluoride reactivity in a myriad of liquid phase organic solvent. Herein, Silicon (Si) anode batteries were constructed with fluoride-based electrolytes to yield optimal ionic conductivity, adequate anode surface activation, current density and electrochemical stability with corresponding cell characterization and operation mechanism. Our novel and functional tools enable optimal utilization of active Si anode-based batteries with complementary advanced cathode materials, bringing forth the next generation of electrochemical energy storage systems based on an active Si anode.

## Introduction

Recent developments in Silicon (Si) RedOx battery designs show a promising path towards deeper understanding of the physiochemical properties of this and many other similar systems.<sup>[1,2]</sup> Proof of concept prompts further investigation towards more sustainable and economic cell configurations. Currently, the rising demand in energy storage devices weighs a toll on available technologies;<sup>[3]</sup> thus, broadening of the scope of possible energy storage technologies. Lithium-ion batteries (LIBs) stand supreme as the leading electrochemical energy storage technology thanks to high energy density, fast kinetics, legacy investment in research and development and established supply chains.<sup>[4,5]</sup> In the venture to increase the breadth of potential technologies, the scientific community is currently in an arms race to utilize other and more widespread elements such as Zn,<sup>[6–9]</sup> Fe,<sup>[10–13]</sup> Mg,<sup>[14–16]</sup> Al,<sup>[17,18]</sup> Ca<sup>[19–22]</sup> and Si.<sup>[1,23–26]</sup> The utilization of more abundant elements enables prioritization of

LIBs in more upscale applications as electric vehicles (EVs) and consumer electronics that require high energy density and quick performing kinetics. Large scale energy storage, high energy and low power applications are a promising niche for novel cell designs with cheaper, more abundant and recyclable materials.

Silicon, as the second most abundant element on earth's crust has shown promising progress in the recent decade.<sup>[1,23]</sup> Cell configurations from primary Si-air cells<sup>[23,25,26]</sup> to more recent advances that provide more insight towards reversible Si RedOx that can be incorporated in secondary (rechargeable) cells. The high energy density of 8.4 kWh kg<sup>-1</sup><sup>[1,26]</sup> makes Si a suitable candidate for high energy applications outside the scope of LIBs in application where they are deemed excessive and warrant investigating varied alternatives. Its sluggish kinetics, embodied in low current densities, limits its usage to low power and high energy electrical applications such as sensors; thus, providing a viable alternative for high end LIBs in lower grade uses and help prioritize current resources and divert supply chains to highly demanded applications. Surface activation was and remains the major hurdle to overcome while utilizing active Si anodes wherein, high concentrations of fluoride deemed necessary for effective passivation removal and oxidative dissolution.<sup>[23,26]</sup> Current methods incorporate fluorinated ionic liquids in Si cell chemistries; wherein, high concentrations of fluoride enable both high ionic conductivity and surface activations in a satisfactory fashion,<sup>[1,18,25,27]</sup> while simultaneously mitigating parasitic corrosion of the Si anode.<sup>[1,25]</sup> Parasitic corrosion is a long persisting detriment in aqueous electrolytes; in which, Hydrogen evolution reduces anode capacity and renders hydrogen gas a safety hazard in long term battery storage.<sup>[9,18,28,29]</sup> This predicament prompts an array of solutions

[a] Dr. A. Epshtain, Dr. I. Baskin, Prof. Y. Ein-Eli  
Department of Materials Science and Engineering  
Technion-Israel Institute of Technology  
Haifa 3200003, Israel  
E-mail: eineli@technion.ac.il

[b] Prof. Y. Ein-Eli  
Grand Technion Energy Program (GTEP)  
Technion-Israel Institute of Technology  
Haifa 3200003, Israel.

Supporting information for this article is available on the WWW under  
<https://doi.org/10.1002/batt.202300571>

© 2023 The Authors. *Batteries & Supercaps* published by Wiley-VCH GmbH.  
This is an open access article under the terms of the Creative Commons Attribution License, which permits use, distribution and reproduction in any medium, provided the original work is properly cited.

ranging from corrosion inhibitors in aqueous electrolytes to organic solvents that provide both wider electrochemical windows (EW) and minimize the Hydrogen evolution reaction. Fluoro-hydrogenate species in particular exhibit relatively low Hydrogen evolution rates depending on concentration and electrolyte water content.<sup>[17,18,24]</sup> Organic fluoride salts were demonstrated to perform surface activations in primary Al-air batteries,<sup>[17,18]</sup> in which, tetra butyl ammonium fluoride tri hydrate (TBAF·3H<sub>2</sub>O) enabled efficient surface activation and satisfactory electrolyte conductivity, as well as being widely implemented as a soluble source of fluorides in organic solvents in the pharmaceutical and chemical industry.<sup>[30–34]</sup> The demonstrated success in battery applications,<sup>[1,17,18,24]</sup> accompanied with the newfound results of the role said species play in surface activation prompt further investigation towards characterization and modeling of novel electrolytic systems for more diverse future applications.

Understanding oligo-fluorinated species behavior in various electrolytic systems stands at the core of unlocking customized cell configurations with tailored properties for given cell chemistries. Physical characterization accompanied by new density function theory (DFT) modeling can illuminate the experimental results and assist in extrapolation towards new cell designs. To the best of our knowledge, species characterization was focused on solid state and gaseous phase analysis.<sup>[35–37]</sup> Liquid phase analysis was focused solely on electrolytic properties,<sup>[27,30,38]</sup> with speciation distribution and its effect on electrolyte performance still lacking in understanding. The main challenge is the wide scope of organic solvents that can be incorporated in various cell designs for which, each material possesses distinct characteristics impacting speciation and solute behavior. Dielectric constants, viscosity, electrochemical window, basicity, donor and acceptor number, to name a few, influence the behavior of the supporting electrolyte. A wide scope of organic aprotic solvents is incorporated in many commercial cell designs, of which the most prominent are carbonate-based solvents.<sup>[18,39,40]</sup> Notwithstanding, a myriad of commonplace solvents can affect solubility,<sup>[39–41]</sup> solvation, kinetics and more importantly, speciation and of electroactive species.<sup>[31,34,42]</sup> The resulting battery design can incorporate Si or even other active metal anodes, conversion cathodes solely constrained by our design and Fluoride-ion based electrolyte,<sup>[43,44]</sup> that facilitate the conversion reaction at the terminal electrodes to culminate also in novel and tailored Fluoride-ion batteries, with compatible materials and vice versa from the perspective of electrode selection for specific applications.

Altogether, a more profound understanding of solvent and solute interaction can advance customized tailoring of electrochemical systems to any specific application, be it high-energy as in sensors or consumer electronics or high-power as in EVs or large-scale grid storage in the venture to prioritize existing resources for each individual use and application. This approach has been detrimental in our previous ventures towards cell design and has culminated in surprising insights elucidating novel RedOx mechanisms and cell operations.<sup>[1,2]</sup> Further

findings will enable more methodic characterization and modeling towards various future cell configurations.

## Results and Discussion

### Targeting high ionic conductivity via systemic study

A set of experiments was performed to characterize electrolyte behavior, in the context of solutes and speciation as they relate to surface activation of passive materials, ionic conductivity and electroactive species stabilization. Fluoro-hydrogenate species play a detrimental role in cell functionality in passive anodic materials,<sup>[1,17,18,25,26]</sup> hence, analytic determination of species distribution and their effect on cell operation is crucial in future cell designs. As established in prior finding,<sup>[24]</sup> high concentrations of fluorides culminate in the formation of electroactive species with high ionic conductivity with effective surface activation.<sup>[1,18]</sup>

One lacking key component in proper understanding of their role in cell operation and species distribution as it pertains to concentration and solute-solvent interactions. Such characterization, to the best of our knowledge, has yet to be established due to high variability of organic aprotic solvents; herein, we set forth the rigorous procedure to characterize, model and implement such findings in an optimal cell design. Table 1 displays a clear correlation between the TBAF·3H<sub>2</sub>O organic electrolyte concentration and ionic conductivity to culminate in a typical maximal conductivity, declining with increased solute concentration due to increasing viscosity. Furthermore, electrolyte translucency and ion chromatography analysis clearly indicate high solubility of the organic electrolyte within the examined concentration range.

Potassium fluoride (KF) was also examined as a potential fluoride source along with C-18-6 crown ether and Triphenyl boron as additives that would enable an increased fluoride ion solubility; the results yielded interesting yet, unsatisfactory results for an application in Si anode based battery applications. The full scope of characterization is elaborated in the supplementary section **Tables S2 and S3** and elucidate many hypotheses regarding fluoride ions speciation in a rather long list of organic solvents. We have observed an increase in KF solubility with the addition of the Lewis acid and base. The same trend was observed in attempts to increase K ion complexation while adding 18-C-6 crown ether. It should be noted that none of the above examined systems achieves satisfactory results.

### Identification of species responsible for increased ionic conductivity

To verify the existence of the oligo-fluorinated species in the examined electrolytes, an Attenuated Total Reflection Fourier Transform Infra-red (ATR-FTIR) spectroscopy was performed. The analysis provides a qualitative measure to the presence of the species and is presented in Figure 1a for a solvent mixture of Ethylene Carbonate (EC) and Propylene Carbonate (PC) 1:1

**Table 1.** Electrolyte physical and electrochemical characteristics.

Solvent	TBAF·3H <sub>2</sub> O concentration [M]	Total [F] via IC [mM]	Ionic conductivity (S m <sup>-1</sup> )
ACN	0.5	510±3	2.61±0.08
	1.0	992±4	3.12±0.04
	1.5	1489±3	2.95±0.05
	2.0	2023±6	2.76±0.02
THF	0.5	493±4	1.12±0.04
	1.0	986±7	1.25±0.03
	1.5	1512±5	1.32±0.02
	2.0	2034±4	1.27±0.03
DMSO	0.5	525±3	0.71±0.02
	1.0	1036±6	0.70±0.05
	1.5	1490±6	0.77±0.03
	2.0	2012±7	0.72±0.02
DMF	0.5	488±5	0.84±0.04
	1.0	987±8	1.06±0.03
	1.5	1516±5	1.12±0.02
	2.0	2024±7	1.11±0.04
PC	0.5	525±6	0.68±0.05
	1.0	984±4	0.91±0.02
	1.5	1533±9	0.75±0.03
	2.0	2044±7	0.61±0.02
EC/PC 1:1 v/v %	0.5	493±5	0.49±0.04
	1.0	1026±3	0.67±0.06
	1.5	1532±9	0.71±0.05
	0.5	1988±5	0.70±0.02
EC/DMC 1:1 v/v %	1.0	512±4	0.68±0.02
	1.5	991±7	0.82±0.04
	2.0	1521±6	0.84±0.04
	0.5	2018±8	0.83±0.05

\*Room temperature 22±0.5 °C.

v/v% with the added TBAF·3H<sub>2</sub>O electrolyte at varied concentrations with corresponding peaks of relevant species, as previously reported in the literature.<sup>[18,45]</sup> The spectra relays increasing absorbance of said species as it pertains to increasing solute concentration, thus further verifying the correlation between fluoride concentration and the tendency toward complexation. The full scope of investigated solutes and solvents is elaborated in the supplementary section **Figures S1** and **S2**. The qualitative results obtained in the ATR-FTIR characterization verify and expand upon previous findings in analogous electrolyte systems.<sup>[17,18]</sup> These findings confirm the

presence and stability of fluoro-hydrogenate species in all electrolyte systems yet, quantitative assessment is yet to be obtained in liquid phase systems; notwithstanding, crystalline and gas phase characterization was previously performed.<sup>[27,35,46,47]</sup>

However, species distribution as it relates to fluoride concentration in solvents, to the best of our knowledge, has yet to be determined. Lack of characterization arises mainly due to vastly disparate chemical environments in each electrolyte system along with a concentration variability which further complicates the problem. Nuclear magnetic resonance (NMR)

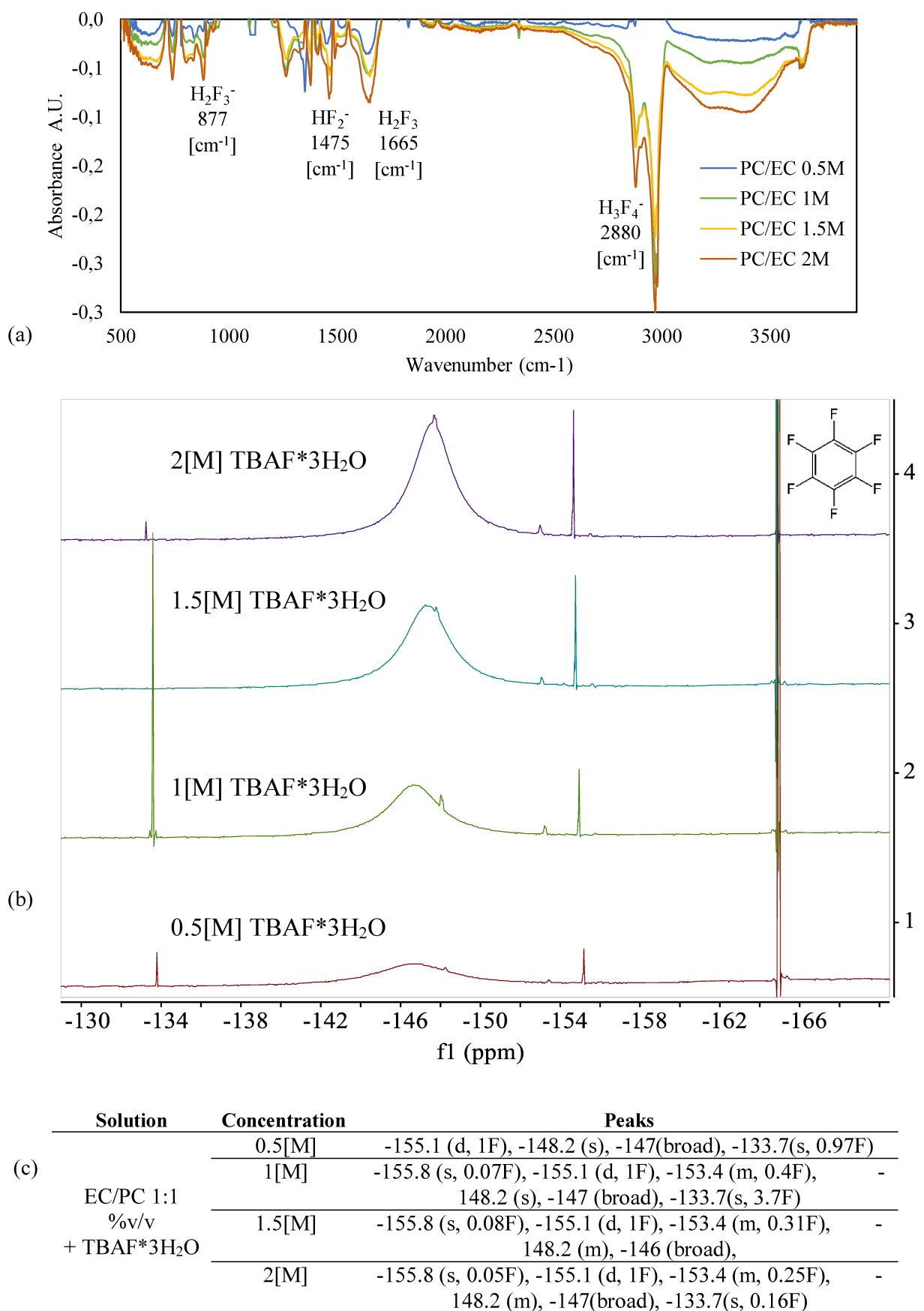


**Figure 1.** a. ATR-FTIR spectra of various electrolytes containing 0.5–2[M] of TBAF·3H<sub>2</sub>O. b. NMR spectra stacks of an array of concentration ranging from 0.5–2[M] TBAF·3H<sub>2</sub>O in EC/PC 1/1 v/v %. c. <sup>19</sup>F NMR peak analysis.

spectroscopy provides the necessary tools to determine species distribution. Figure 1b and c displays an array of  $^{19}\text{F}$  NMR spectra stacks of concentration ranging from 0.5–2[M] TBAF·3H<sub>2</sub>O in EC/PC 1/1 v/v%, and show the characteristic shifts of fluoro-hydrogenate species in accordance with previous studies.<sup>[30]</sup> Quantitative NMR was performed to utilize peak integration with no clear identifiable peak at lower shifts (below <90 ppm), associated with free fluoride ions,<sup>[44,48]</sup> indicating Fluorine oligomerization. Lastly, a clear wide peak is apparent in all spectra, indicating chemical environment shifts at a time scale faster than the scan rate, in a similar manner to hydrogen bonded protons in  $^1\text{H}$  NMR spectra with increasing integration area. The presence of a wide peak correlates with the reported structure in fluorinated ionic liquids, in which HF acts as a dielectric spacer rapidly exchanging sites, thus contributing to the overall electrolyte conductivity.<sup>[37]</sup> Unfortunately, the presence of a wide peak bars quantitative peak integration as it pertains to speciation distribution on the one hand yet, on the other hand it further emphasizes the high ionic conductivity obtained these electrolytes. The full scope of solvents along with a set of Potassium fluoride (KF) electrolyte systems including characterization thereof are elaborated in the supplementary section **Figures S3–S5** and **Tables S4–S5**.

## Predictive methods of physical characteristics

### Chemical environment and complex dissociation

We have evaluated the propensity of the fluoride anion to form complexes with HF molecules in the gas phase and several solutions using both the SMD and the IEFPCM methods. To this end, the complexation free energy was estimated as the difference between the formation free energy of the fluoro-hydrogenate anion and the sum of the formation free energies of its components (F<sup>-</sup> and HF). The values obtained using SMD for (FH)<sub>n</sub>F<sup>-</sup> and all solvents involved in the study are presented in the supplementary section **Tables S6–S8** and **Figure S7**. The

effect from the addition of each subsequent HF molecule to the complex decreases as  $n$  increases as portrayed in Figure 2a. It stands to notice that although the absolute complexation free energy in vacuum increases significantly with the addition of each HF molecule, in solutions, the addition of the third HF molecule gives a significantly smaller gain in free energy. Therefore, it can be expected that a simultaneous presence of comparable amounts of (FH)<sub>2</sub>F<sup>-</sup> and (FH)<sub>3</sub>F<sup>-</sup> could be found in the solution. This may relate to the fact that in ionic liquids, formed by complete saturation of (FH)<sub>n</sub>F<sup>-</sup>,  $n$  often takes a value close to 2.3, which corresponds to a mixture of (FH)<sub>2</sub>F<sup>-</sup> and (FH)<sub>3</sub>F<sup>-</sup> in a ratio of 7:3.<sup>[49]</sup> Note that in the gas phase, the difference in free energy is still quite large (>14 [kcal mol<sup>-1</sup>]); therefore, the convergence of free energies is a consequence of the electrostatic interaction of solute anions with the polarizable solvent medium.

Table 2 contains the values of the dissociation free energy of HF from fluoride-anion complexes in different solvents, which can be calculated from the formation free energy values elaborated in the supplementary section **Table S7**. It shows several regularities very clearly; in particular, the free dissociation energy of HF decreases significantly with an increase in the number of HF units in the complex, as well as when moving from the gas phase to a solvent. Furthermore, Table 2. displays low values of the dissociation free energy in polar solvents for (FH)<sub>2</sub>F<sup>-</sup> and very low values for (FH)<sub>3</sub>F<sup>-</sup>. This explains several experimental facts shown in Figure 1 and Table 1. In particular, since two reversible processes of HF cleavage from these two complexes and their reverse binding are quite sufficient for a very fast mutual exchange of terminal and central Fluorine atoms even at low temperatures, any  $^{19}\text{F}$  NMR spectrum for these complexes and their mixtures should be a very broad singlet, in agreement with the literature data<sup>[27]</sup> and the experimental results. In addition, it is these processes of easy HF units exchange between complexes,<sup>[47]</sup> that forms the basis of this mechanism leading to high ionic conductivity. As follows from the calculations, very low free dissociation energies lead to high ionic conductivity and can be theoretically predicted by

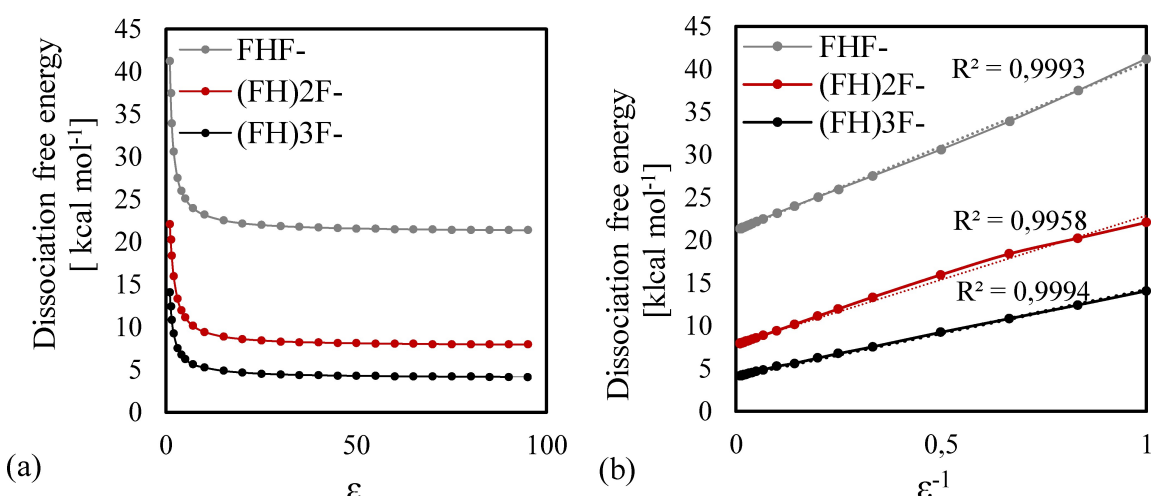


Figure 2. Dependence of the dissociation free energy estimated using IEFPCM on: a. the dielectric constant. b. the reciprocal dielectric constant.

Dissociation reaction	gas	ACN	DMF	DMSO	PC	THF	EC:PC	EC:DMC
FHF <sup>-</sup> → F <sup>-</sup> + HF	41.6	17.8	17.8	17.7	17.6	20.8	17.6	17.7
(FH) <sub>2</sub> F <sup>-</sup> → FHF <sup>-</sup> + HF	22.1	5.4	5.6	5.4	5.3	7.5	5.3	5.4
(FH) <sub>3</sub> F <sup>-</sup> → (FH) <sub>2</sub> F <sup>-</sup> + HF	14.1	0.6	2.2	2.2	3.4	2.3	1.7	2.1

solely including interaction with the polarizable medium in quantum chemical calculations. It also follows from Table 2. that the reversible dissociation of the FHF<sup>-</sup> complex, leading to the exchange of Fluorine atoms between this complex and fluoride anion, should be a much slower process, but quite possible at room temperature. Therefore, at a certain temperature range it could lead to line broadening in the <sup>19</sup>F NMR spectrum due to dynamic exchange of Fluorine atoms.

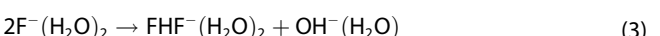
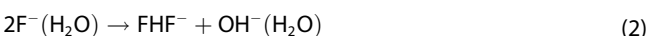
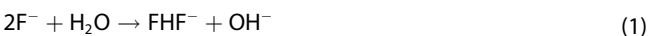
### Basicity of the fluoride anion and its "nakedness"

The concept of a "naked" fluoride anion comes from synthetic organic chemistry and denotes a fluoride anion in aprotic solvents, with which it does not form hydrogen bonds or coordination bonds forming its "clothes" and is therefore called "naked", and acts as a very strong base and nucleophile.<sup>[43,48,50–52]</sup> Evidently, a consequence of the highest electronegativity among all elements and its small atomic radius, which leads to the formation of very strong Hydrogen bonding.<sup>[31]</sup> Although opening new synthetic possibilities in organic chemistry, this phenomenon may turn out to be undesirable in electrochemistry, since it can lead to the destruction of organic components in the electrolyte. However, its basicity and nucleophilicity can be significantly reduced in protic solvents by forming hydrogen bonds with the fluoride anion to yield oligofluorinated species. Important to note that despite the practical importance of this phenomenon, to the best of our knowledge, there are no theoretical works devoted to its systematic study in the literature. Herein, we applied computational methodology as discussed above to model this phenomenon. The predicted changes in free energy in the acid-base reactions depicted in Eq. (1)–(3). for the gas phase and the seven solvents involved in this study (estimated using SMD) are elaborated in supplementary section Table S9.

Computation of the change in free energy in three acid-base reactions as depicted in Equations (1)–(3) exemplifies the basicity of the fluoride anions and its complexes with limited stoichiometry of water molecules as implemented experimentally in this study via TBAF·3H<sub>2</sub>O as a soluble source of fluorides. The spatial structures of the four complexes with water molecules in the gas phase, as a reference point, are shown in Figures 3c–f. Important to note that unlike the non-hydrated bifluoride FHF<sup>-</sup>, which has a symmetrical structure with equal F–H bond lengths, the hydrogen bond in its hydrated complex FHF<sup>-</sup>(H<sub>2</sub>O)<sub>2</sub> is no longer symmetrical (the F–H distances are 1.076 Å and 1.213 Å in the gas phase), which is a consequence

of the interaction of two H<sub>2</sub>O molecules with each other. With an increase in the dielectric constant of the medium, the difference in these distances decreases, yet the structure remains asymmetric with F–H distances 1.100 Å and 1.173 Å at  $\epsilon=80$ . To an even greater extent, such changes affect the structure of the complex of hydroxide anion with a water molecule OH<sup>-</sup>(H<sub>2</sub>O), which in the gas phase has an almost symmetrical structure with O–H distances of 1.219 Å and 1.222 Å, while in a polar medium it becomes highly asymmetric with O–H distances of 1.083 Å and 1.389 Å at  $\epsilon=80$ .

Acid-base reactions exemplifying the basicity of the fluoride anion and its complexes with water molecules with respect to water.



The results of these calculations make it possible to analyze the deactivation of fluoride anions by placing them in a solvent and changing its dielectric constant. Such analysis can be carried out based on the data in changes in the free energies of the acid-base reactions (1)–(3). on the dielectric constant of the medium as presented in Figure 3a–d. From Figure 3e the course of the curve corresponding to the acid-base reaction(1). indicates a sharp deactivation of the naked fluoride anion with an increase in the dielectric constant, and its basicity evens out with the basicity of the hydroxide ion already present in a weakly polar medium at a relatively small value  $\epsilon=5$ . With a further increase in the dielectric constant, the fluoride anion becomes a weaker base compared to the hydroxide, and as a result, the thermodynamic equilibrium is shifted towards the predominance of fluoride anions in the solution, which corresponds to previous results.<sup>[31]</sup>

Nevertheless, the difference between the free energies of the fluoride F<sup>-</sup> and bifluoride FHF<sup>-</sup> anions, according to the calculations using IEFPCM, remains small, not exceeding 2.8 (kcal mol<sup>-1</sup>) even for very polar solvents with  $\epsilon=80$ . This means that in an aprotic solvent, even with high values of the dielectric constant, the "naked" fluoride anion is only partially deactivated, and it is still a sufficiently strong base and nucleophile capable of leading, among other things, to the decomposition of certain organic components of the electrolyte as previously reported.<sup>[43]</sup> On the other hand, this may indicate the presence of a fluoro-hydrogenate species in the solution.

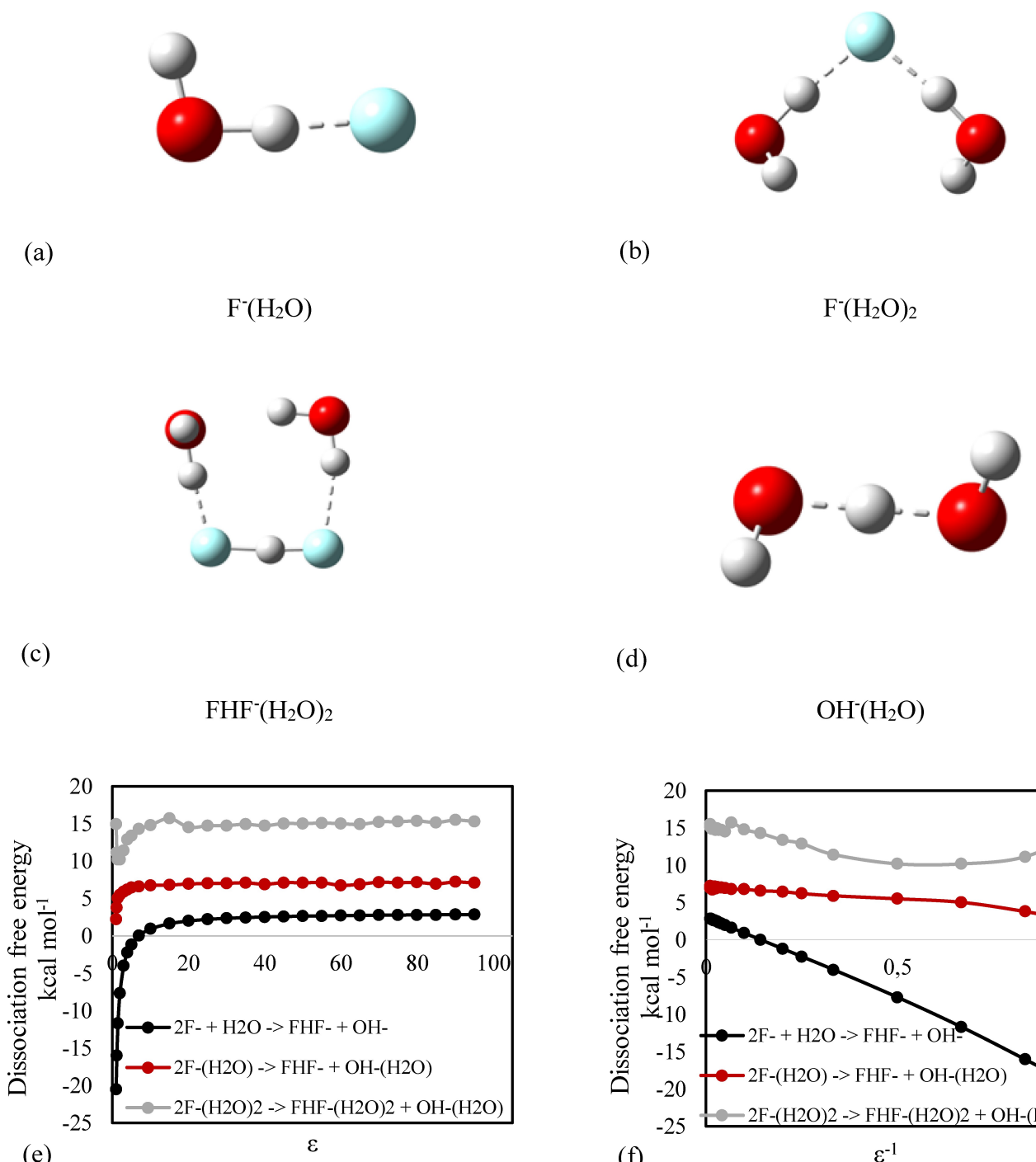


**Figure 3.** Dependence of the change in free energy in acid-base reactions on: **a**. the dielectric constant; **b**. the reciprocal dielectric constant; **c-f**. the hydration of species under the same conditions.

From Figure 3f the dependence of the change in free energy on the reciprocal values of the dielectric constant additional features are visible. First, a strong dependence of fluoride basicity on the polarity of the medium is observed only for the “naked” anion, while with the addition of one and especially two water molecules, the dependence weakens and becomes more complex. This means that complexation with water molecules in its immediate vicinity, creates its own polar

environment near the fluoride anion, partially replacing the solvent environment. Thus, the aforementioned considerations explain first, the sharp change in the basicity and nucleophilicity of the anion during the transition between protic and aprotic solvents, regardless of their polarity, that is, the phenomenon of fluoride ions “nakedness”. Secondly, why the addition of even a small amount of water to a solution of a fluoride salt in an aprotic solvent can lead to the same deactivation of the “naked”

anion as substitution to a protic solvent i.e. water; hence, we can enjoy high solubility, conductivity and stability with minimal concentration of water whilst mitigating its adverse effects on electrolyte stability. Further experimental proof of electrolyte stability can be found in the supplementary section **Figures S8–S10** and **Tables S10–S13** depicting the GC-MS analysis of the PC/EC electrolyte with 2[M] of TBAF·3H<sub>2</sub>O.

### Macroscopical molecular dynamics

To conduct a detailed structural analysis of the liquid electrolytes used in this study, we performed molecular dynamics (MD) simulations of the electrolytes based on the EC:PC 1:1 v/v % solvents mixture for four different concentrations of TBAF: 0.5, 1.0, 1.5, and 2.0 M, as experimentally implemented herein. The methodology of MD simulations is described in the experimental section. The composition of the simulation boxes used in these studies, along with several equilibrium characteristics of the boxes, are disclosed in the supplementary section **Table S14**.

Figure 4a shows the last frame from a 2 (ns) MD trajectory for a 0.5[M] TBAF·3H<sub>2</sub>O solution in an EC:PC 1:1 v/v% mixture. To avoid piling up a large number of atoms (about 3000 atoms in the modeling box) and to simplify the analysis, there are no solvent molecules in the figure, and their locations are indicated by a set of light dots in two colors, denoting solvent molecules of two types, EC and PC. Figure 4a clearly shows four types of complexes formed by fluoride ions: i) an ordinary complex with water molecules, ii) a solvent-separated ion pair, iii) a contact ion pair, and iv) a bridged binuclear Fluoride hydrate, marked with the letters A–D. Complexes of the latter type have a very unusual structure: in them, three water molecules act as a bridge that connects two anions and thereby binding them into a single hydrated complex. To the best of our knowledge, the possibility of the formation of such complexes upon solvation of fluoride anions was not previously considered in the literature. It can be assumed that their formation could be associated with a lack of water molecules in the solution; therefore, water molecules begin to use both of their protons to form hydrogen bonds.

Result analysis of the MD simulations show that with an increase in TBAF·3H<sub>2</sub>O concentration, the proportion of such binuclear hydrates increases, trinuclear and even tetranuclear hydrates appear, all of which held together by bridging water molecules. Figure 4b shows the spatial structures of polynuclear hydrates containing two to four Fluorine atoms, extracted from the results of the MD simulations of TBAF·3H<sub>2</sub>O solutions in EC:PC 1:1 v/v%. These polynuclear hydrates are similar in structure to ion channels in cell membranes, inside the channel there are negatively charged fluoride ions, the walls of the channel are formed by bridging and non-bridging water molecules, the positive end of which is directed inside the channel, stabilizing the negative charge of the anions, and the negative end of the dipole is directed outward, to the positively charged TBA cations. It is also important to note that the simultaneous presence within such complexes in a small

volume of several fluoride anions and a large number of water molecules creates very favorable conditions for their reaction with each other with the formation of the bi-fluoride FHF<sup>-</sup> and other fluoro-hydrogenate anions. This model can explain the continuous ability to activate the surface of an active metal electrode despite the presence of a significant amount of water molecules in the solution, as previously reported in metal anode batteries.<sup>[17,18]</sup>

To estimate the proportion of fluoride anions included in the composition of polynuclear Fluoride hydrates, in the last frame of the MD trajectory, we calculated the full set of interatomic distances considering periodic boundary conditions, counting for each Fluorine atom the number of other Fluorine atoms that are less than 3.5 Å away (since it corresponds to the distances between neighboring atoms in such multinuclear complexes). Allowing an estimate of the proportion of anions included in such complexes, both with any number of nuclei (fluorine atoms) and in large complexes with three or more Fluorine atoms. The dependence of these two indicators on the concentration of TBAF in a solution is shown in Figure 4c. It can be seen that a significant part of the fluoride anions take part in such complexes, reaching a maximum at a concentration of 1.5 (mol l<sup>-1</sup>). At the same time, the proportion of Fluorine atoms included in large complexes with three or more nuclei increases monotonically as the concentration TBAF increases.

Using a similar technique based on counting the distance between Fluorine and Hydrogen atoms, the number of water molecules that form a Hydrogen bond with each of the fluoride anions was counted, *i.e.* their coordination number with respect to water molecules. Figure 4d. shows the histogram of the distribution of coordination numbers for fluoride anions with water molecules. The coordination number can take any value less than or equal to six. Hence, they cannot be considered completely naked, since they form weak hydrogen bonds with solvent molecules; nevertheless, higher reactivity can be expected.

Also, an estimate of the average value of this coordination number depending on the salt concentration, performed in two ways. First, averaging the data shown in the histogram in Figure 4d (method 1). Second, the average coordination number over a two (ns) trajectory based on the radial distribution function, using the PyLAT tool (method 2). The dependence of the average coordination number on the TBAF concentration is shown in Figure 4e. It can be seen that despite the difference in the methods determining the coordination number, the results obtained are congruent. In particular, the maximum value of the average coordination number is achieved at a salt concentration of 1.5[M] in accordance with the experimental data. Lastly, it is important to note that the value of the average coordination number in most cases is above three and reaches four at some concentrations. Since in the electrolyte itself there are only three water molecules for each fluoride anion, average coordination numbers exceeding three can be explained by the fact that bridging water molecules are coordinated as well, forming hydrogen bonds, with two fluoride anions at once, as water-bridged polynuclear hydrates. Quantum-chemical modeling of water-bridged poly-

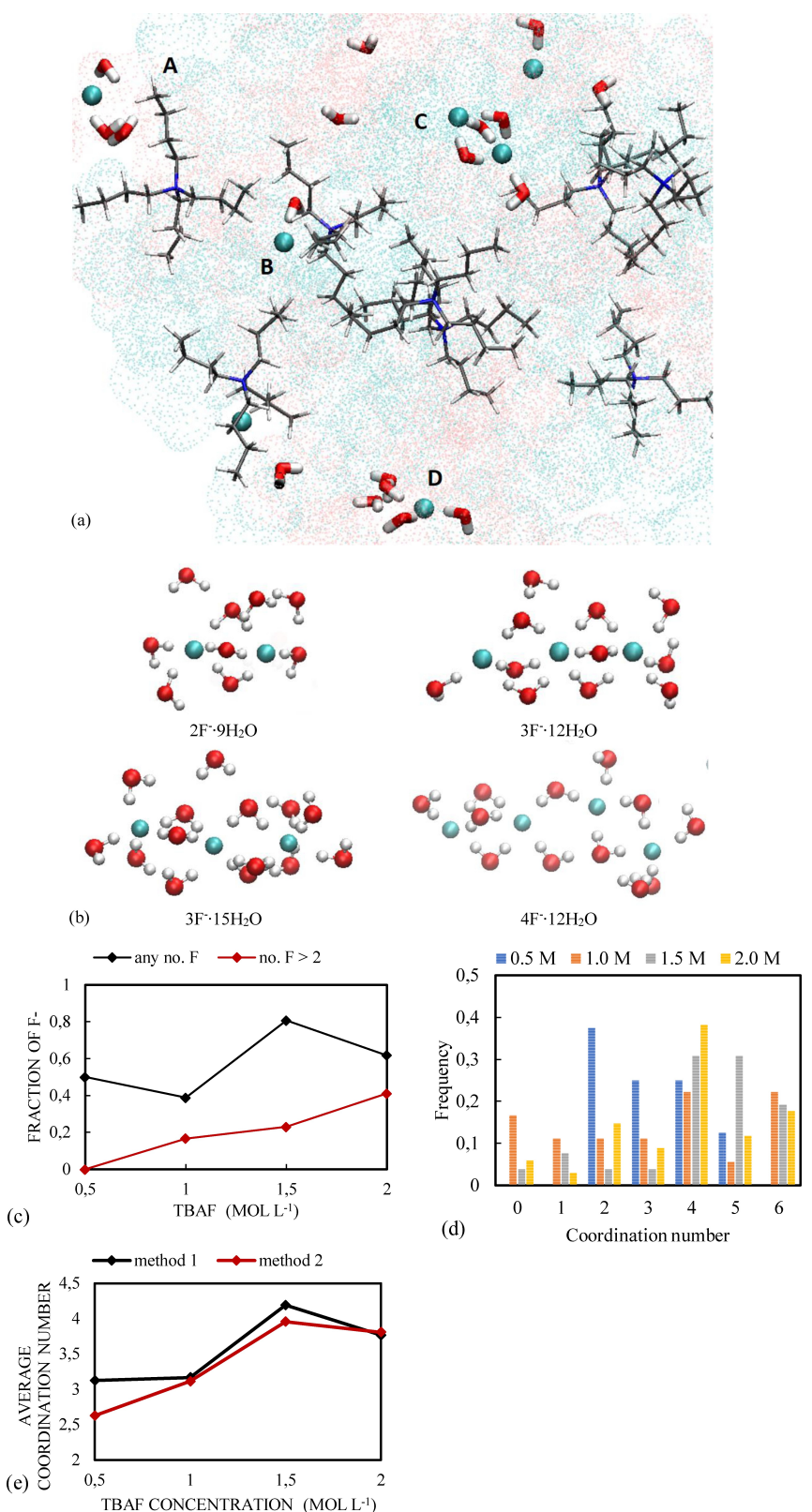


**Figure 4.** a. The last frame from a 2 (ns) MD trajectory for a  $0.5[\text{M}] \text{TBAF}\cdot 3\text{H}_2\text{O}$  solution in an EC:PC 1:1 v/v% mixture. Labels: A – a solvent-separated ion pair; B – a contact ion pair; C – a bridged binuclear fluoride hydrate; D – complex of a fluoride anion with several water molecules; b. Spatial structures of different bridged polynuclear fluoride hydrates extracted from MD trajectories; c. The dependence of the fraction of the fluoride anions in water-bridged polynuclear hydrates on the concentration of TBAF; d. Histogram of the distribution of coordination numbers for fluoride anions in their coordination with water molecules; e. The dependence of the average coordination number on TBAF concentration

nuclear fluoride hydrates can be found in the supplementary section **Figures S11**.

### Predictive chemical characteristics

We have explored the possibility of modeling the solvent effect on NMR spectra using both the continuum and atomistic approaches. Table 3 shows the  $^{19}\text{F}$  chemical shift values predicted while considering the solvent effect using the SMD continuum model. As can be seen this approach leads to the prediction of almost the same chemical shift value for  $\text{F}^-$ ,  $\text{HF}^-$  and  $(\text{FH})_2\text{F}^-$  for all solvents, which clearly contradicts the experimental data, as seen in the literature<sup>[48]</sup> and the results in Figure 1. The NMR calculation is based on the electrostatic model of charge interaction with a polarizable medium, although it reproduces the free energy of solvation well, it is utterly unsuitable for modeling NMR spectra, since the screening of nuclei is determined by factors other than free energy. For the same reason, other continuum methods based on electrostatic interactions of charges with a polarizable medium, such as IEFPCM, are also not suitable for this purpose. Therefore, to consider the influence of the solvent on the NMR spectrum, one should prefer the atomistic approach based on the explicit consideration of the electronic properties of the spatial structure of superamolecular clusters formed during the interaction of a solute and a solvent.  $^{19}\text{F}$  NMR shifts in Fluorine-containing species and their complexes with water molecules were computed as described in the experimental section 2.7. The results obtained for the gas phase are presented in the supplementary section **Table S15** and **Figure S12**.

A different empirical scheme was utilized, based on a linear correlation between the calculated and observed chemical shift values presented in Figure 5, enabling more accurate predictions. To construct this correlation, utilization of published data on the chemical shift of Tetramethylammonium fluoride solutions in various solvents, assuming that the replacement of the Tetramethylammonium cation by TBA in a dilute solution should not lead to significant changes in the chemical shift of the fluoride anion. To this end, simulation of the complexes of fluoride anions with both the solvent molecules involved in this study (ACN, DMC, DMF, DMSO, EC, PC, and THF) as illustrated in Figure 5a and with additional solvents depicted in **Figure S13** in the supplementary section. The inclusion of which was necessary to build the correlation. In the presence of several complexes for the same solvent, the data for the most stable

complex with the most negative binding free energy was used to construct the correlation equation, and in the presence of several experimental values, all data sets were used. The fact that all calculations were carried out using exactly the same methodology, made it possible to use the constructed correlation to correct the model for the solvents involved in this study. Values of the binding free energy, calculated, corrected, and observed values of  $^{19}\text{F}$  NMR shifts for all complexes involved therein are elaborated in the supplementary section **Tables S15** and **S16**, and their spatial structures are given in Figure S13. The regression line between the experimental and computational results are depicted herein in Figure 5b. Calculated and experimental  $^{19}\text{F}$  NMR shifts.

Altogether, these improved computational models allow more efficient NMR shift predictions and characterization thereafter. In this instance the sum of our modeling, guided by the experimental data, further extrapolated, predicts that a mixture of EC/PC 1:1 v/v% with at least 1.5 [M] of TBAF·3H<sub>2</sub>O is the most suitable electrolyte for high ionic conductivity, electrolyte stability and rapid oligo-fluorinated species reformation in situ, all major requisites for adequate Si anode surface activations and electrodissolution. Hence, these predictions will be verified experimentally in a functional cell design.

### Practical application of the modeled electrolytes

With optimal electrolyte parameters at hand along with supporting predictive modeling, electrolyte performance was tested in active Si anode configurations. Surface activation of Si is a prerequisite in Si RedOx electrochemical cells. The native oxide presiding on the surface, greatly increases the impedance, bars efficient Si oxidative dissolution and reduces the maximal current density, in an already sluggish RedOx kinetics.<sup>[24,26]</sup> Open circuit potential experiments were performed for all the examined electrolytes to test the efficacy of surface activation in each electrolyte and solute concentration. The optimal set of results is displayed in Figure 6a coincides with the predictive modeling and shows rapid and prolonged surface activation, increasing with electrolyte concentration. The full scope of electrolyte testing is elaborated in the supplementary section **Figures S14** and **S15**.

Potentiodynamic experiments displayed in Figure 6b confirm the optimal electrolyte as it pertains to maximal current density, coinciding with the predictive model, determining 1.5[M] as the optimal concentration. The accompanied electro-

**Table 3.**  $^{19}\text{F}$  NMR shifts predicted while considering the solvent effect using the SMD model.

Species	gas	ACN	DMF	DMSO	PC	THF	EC:PC	EC:DMC
$\text{F}^-$	-312.1	-312.3	-312.3	-312.3	-312.3	-312.3	-312.3	-312.3
$\text{HF}^-$	-228.7	-229.3	-229.3	-229.3	-229.3	-229.2	-229.3	-229.3
$(\text{FH})_2\text{F}^-$	-197.9	-197.4	-197.4	-197.3	-197.3	-197.2	-197.3	-197.3
$(\text{FH})_3^{19}\text{F}^-$	-179.4	-180.3	-180.3	-180.3	-177.4	-178.2	-177.8	-177.8
HF	-243.1	-254.3	-254.3	-254.4	-254.6	-252.6	-254.6	-254.4

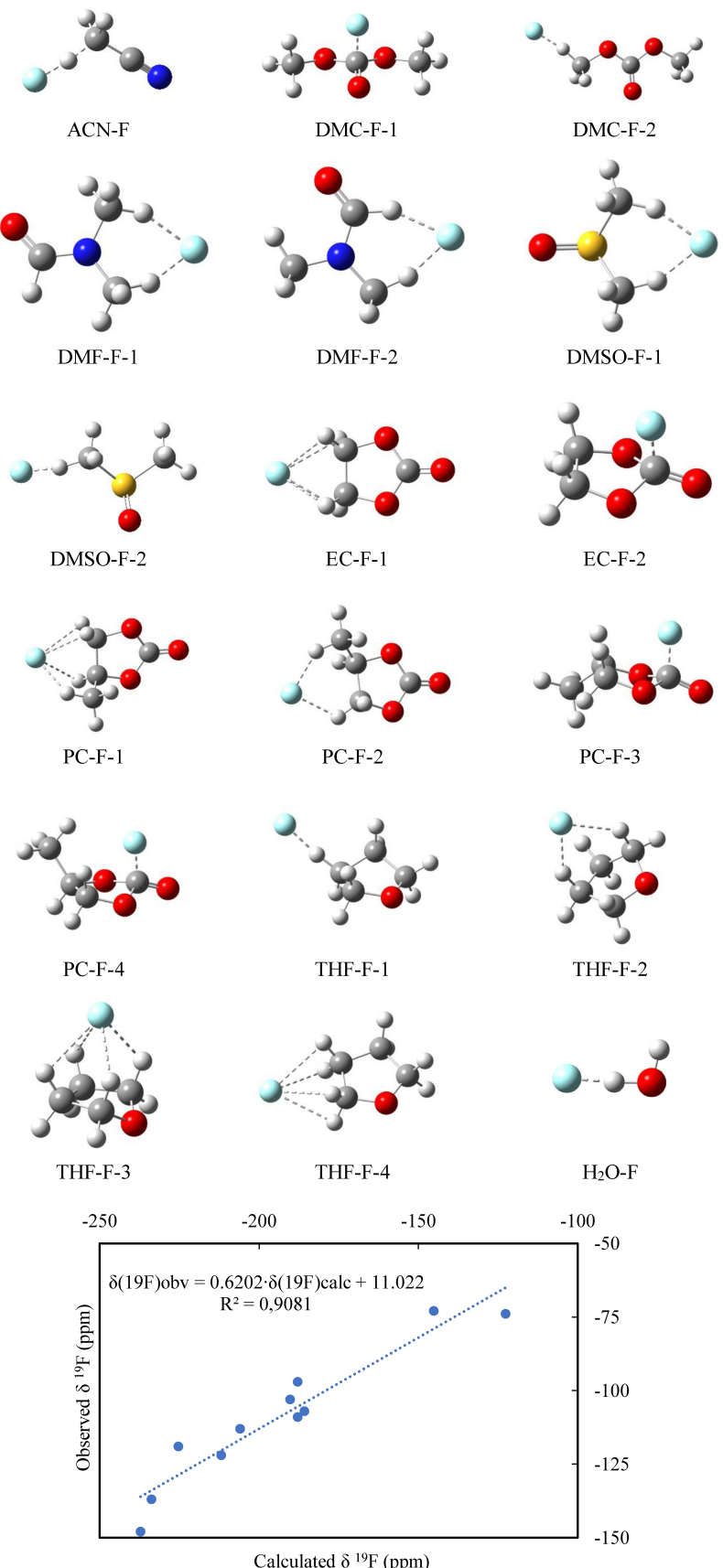
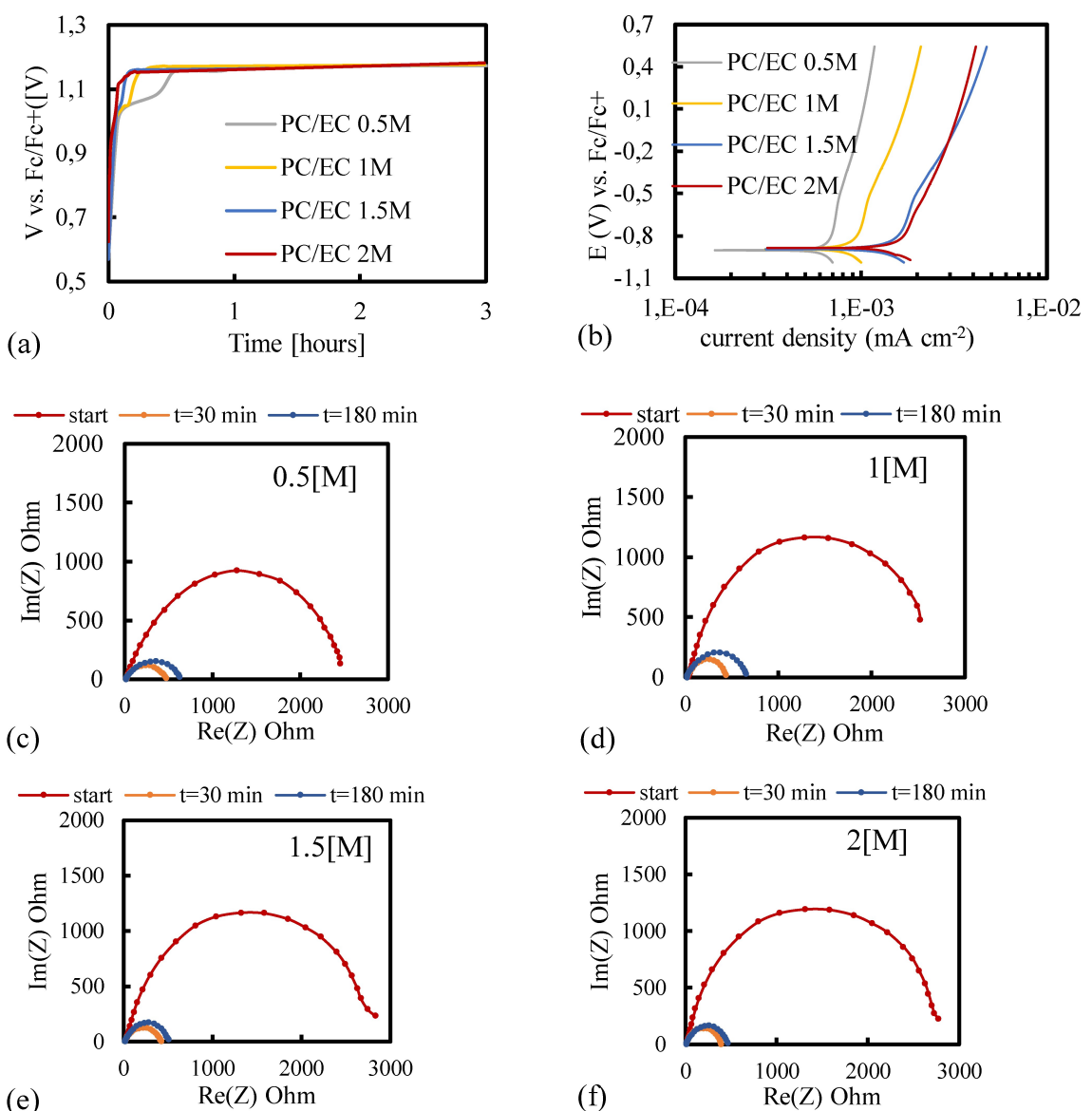


Figure 5. a. Solvation modeling for fluoride anion shift prediction in varied solvents; b. a correlation between calculated and observed values of  $^{19}\text{F}$  NMR shifts.



**Figure 6.** a. Open circuit potential measurements of all tested electrolyte systems via two electrodes configuration utilizing a Si wafer vs. Fc/Fc<sup>+</sup> on a Pt wire; Inlets. b. Potentiodynamic experiments of all tested electrolyte systems. All scan rates were 5 mV s<sup>-1</sup>; c-f. Electrochemical impedance spectroscopy measurements of 0.5–2 [M] TBAF·3H<sub>2</sub>O respectively. Si<sub>n++</sub> wafer as a working electrode W. E.; Platinum foil as a counter electrode C.E; Fc/Fc<sup>+</sup> on a Pt wire as a reference electrode.

chemical impedance spectroscopy in Figure 6c-d starting at the point of contact, 30 minutes and 180 minutes of a Si wafer submersion in TBAF·3H<sub>2</sub>O containing electrolytes clearly displays surface activation in under 30 minutes. Charge transfer impedance precipitously drops upon Si wafer immersion in TBAF·3H<sub>2</sub>O containing electrolytes. However, the drop is followed by an increase after 3 hours, similarly to previous studies concluding partial passivation reformation in metal anode cell configurations.<sup>[17,18]</sup>

These experimental results reinforce the astounding predictive capability of the DFT model and its derived conclusion towards preferential solvents and concentrations for optimal complexation, conductivity, electroactive species and RedOx

kinetics to produce the best cell performance in a novel cell design scheme.

#### Full cell assembly

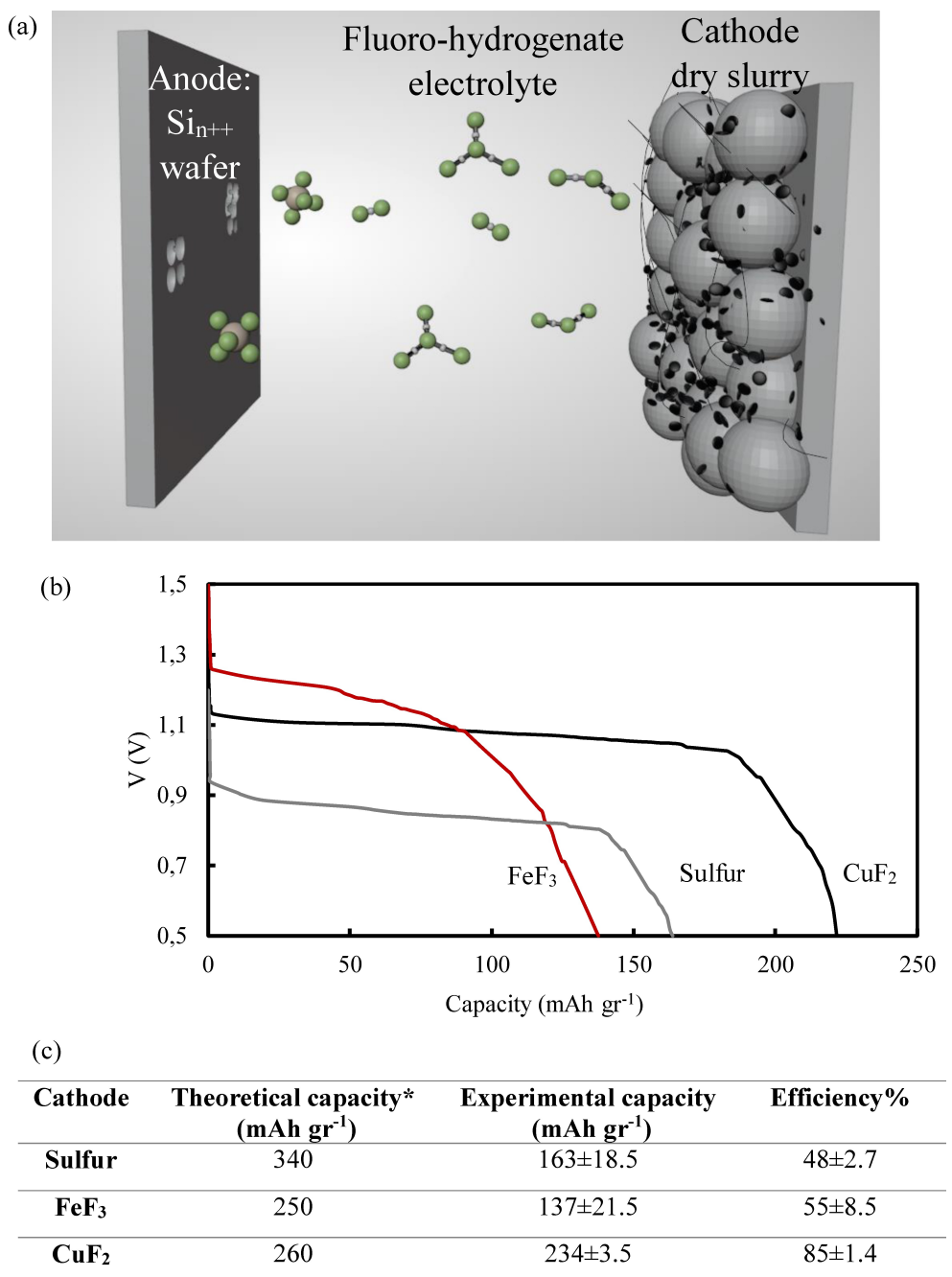
The high degree of sensitivity to oxides, that passive materials such as Si exhibit,<sup>[1,24]</sup> necessitate an oxide free medium. The deleterious effect of water and oxide content in the electrolyte on surface activation must be mitigated and offset; a similar requirement can be made from potential cathodic materials. Following recent advances in Si RedOx cell designs.<sup>[1,2]</sup> a major prerequisite was established, oxide free cathodic materials. The use of fluorides, Halides or Sulfur based cathodic materials

yielded favorable results is proper cell operation. Hence, a range of potential slurry-based cathodes were incorporated in a full cell configuration as illustrated Figure 7a.

### Galvanostatic experiment

Figure 7b lays forth select galvanostatic experiments in a full cell configuration with the optimal electrolyte EC/PC 1:1 v/v% with 1.5[M] of TBAF·3H<sub>2</sub>O, a Si<sub>n++</sub> wafer anode and varied

slurry-based cathodic materials. The full scope of materials examined for compatibility and the assembly process are elaborated in the supplementary section Tables S17–S18. A clear optimal cathode can be deduced from the galvanostatic experiment; wherein, vastly disparate results were obtained with different cathodic materials. CuF<sub>2</sub> emerges as the most compatible material, both for stability and experimental capacity. It was not possible to charge the assembled cells, as they reached limiting voltage within less than a minute due to electrolyte degradation.



\*Calculated based on 1e<sup>-</sup> transfer with regards to the cathodic material as a limiting factor.

**Figure 7.** a. Illustration of the  $\text{Si}_{\text{n}++}$  cell with a slurry-based cathode and electroactive species in the electrolyte; b. Galvanostatic experiments of all successfully assembled cells; c. Cells data including coulombic efficiency as calculated from a series of identically assembled cells.

**Cell characterization****Changes in cathodic materials**

The selected cathodes were examined via X-ray Diffraction (XRD) analysis, as presented in Figure 8 to validate changes in phase as it pertains to the galvanostatic process. Presence of different phases was detected as well as reduction in relative intensities of others, particularly Sulfur. Aluminum foil was used as the current collector and is marked in the measurement. Discharged CuF<sub>2</sub> shows presence of metallic copper, indicating electro-reduction, corresponding with previous applications of CuF<sub>2</sub> as a cathodic materials.<sup>[1,53]</sup> The Sulfur cathode XRD spectra shows signs of crystalline sulfur degradation and structure distortion, indicating phase change during the discharge process as well as the well documented sulfur shuttling

phenomena.<sup>[54,55]</sup> FeF<sub>3</sub> showed clear signs of dissolution after the galvanostatic experiments, as the slurry electrode dissolved thereafter, indicating chemical instability after discharge; thus, could not be compared to long-term storage conditions.

The characterization results imply that the arising half-cell reactions are anticipated to be:

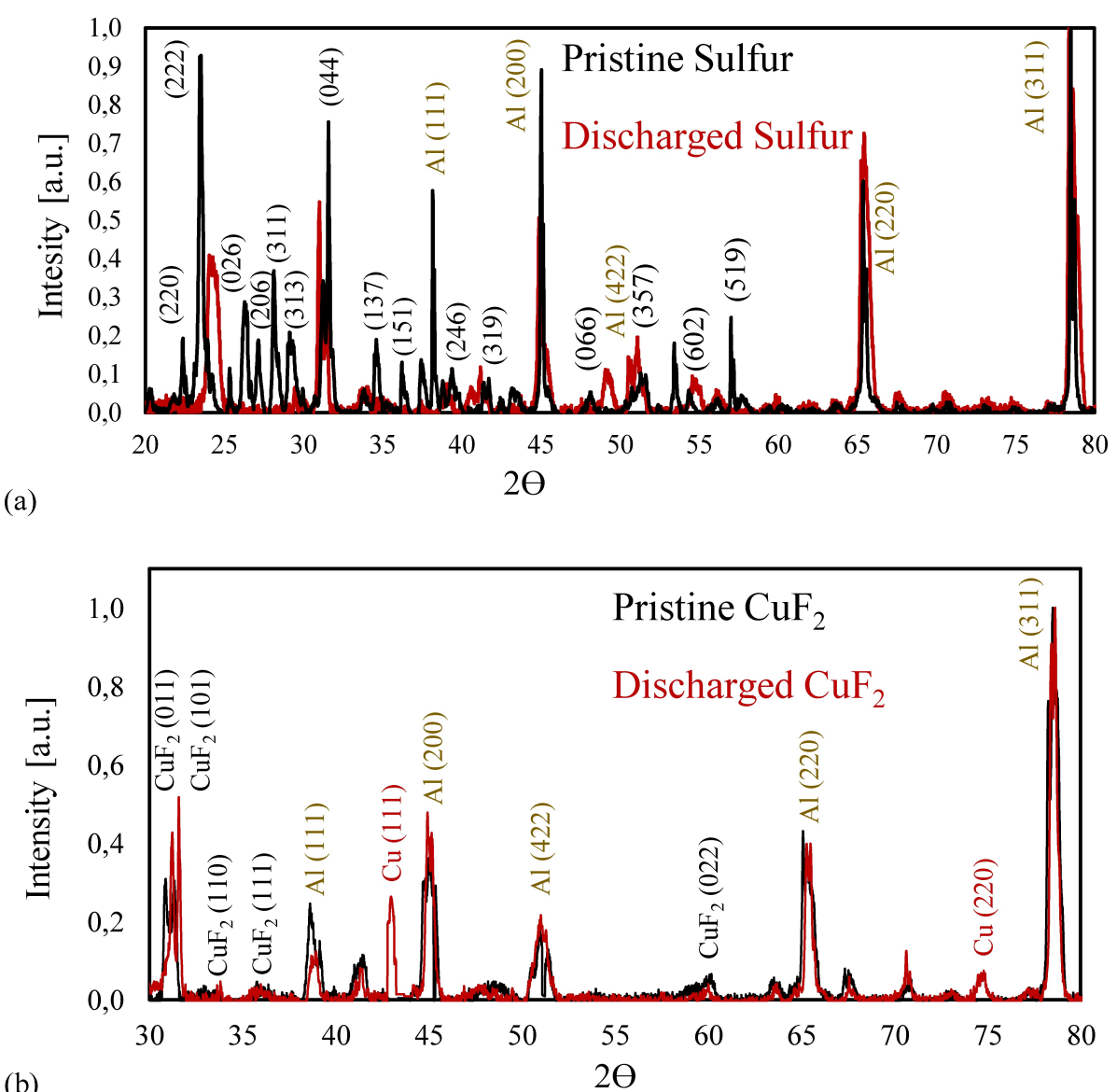
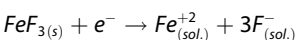
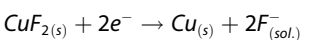
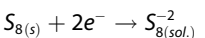


**Figure 8.** XRD spectra of the cathodes in pristine condition and after operational termination following galvanostatic experiments: **a.** Sulfur cathode; **b.** CuF<sub>2</sub> cathode. ·FeF<sub>3</sub> could not be compared due to cathode dissolution after the galvanostatic experiment.

### Changes in Electrolyte Solutes

The electrolytes were characterized via Inductively Coupled Plasma (ICP), the results in Table 4 display a clear distinction between the cathode materials. Solubility was measured both prior to discharge in long term storage, at 50% D.O.D as established by a series of identical galvanostatic experiments after cell operational termination. The discrepancy that arises from these measurements provides more insight toward material stability and solubility in the optimal electrolyte.  $\text{CuF}_2$  shows appreciable stability both during long term storage and operation. Whereas,  $\text{FeF}_3$  displays relative stability in long term storage yet, during discharge the cathode material degrades and dissolves to such an extent that the electrode completely dissolves in the electrolyte and detaches from the current collector. Subsequently, Sulfur displays reasonable stability during storage; however, post discharge there is evidence regarding Sulfur dissolution. Shuttling, a common mechanism of Sulfur dissolution has long been documented, in Sulfur cathode batteries,<sup>[54,55]</sup> hence, a similar hypothesis can arise in this case. As it pertains to the Si anode, an appreciable concentration of dissolved Silicon is apparent post galvanostatic experiments. Contrary to previous studies,<sup>[1]</sup> Si electro-dissolution products appear in the electrolyte further emphasizing the critical role the solvent plays in Si RedOX reactions and the resulting products. Hence, further modeling is in order for proper prediction of material stability as these experimental results help focus the scope of cell designs and optimization.

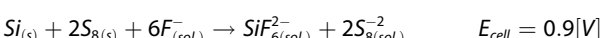
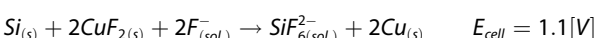
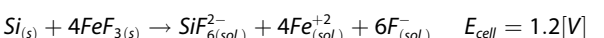
### Modifications and alteration in the Si anode

Lastly, to achieve a multi-faceted image of cell operation and long-term storage, surface analysis of the  $\text{Si}_{n++}$  wafers was conducted via Scanning Electronic Microscopy (SEM). Figure 9 portrays the surface evolution of a  $\text{Si}_{n++}$  wafer in the constructed cell. For reference, a polished  $\text{Si}_{n++}$  wafer is

displayed in Figure 9a. The exhibited etching in Figure 9 d-f shows clear signs of electro-dissolution under anodic polarization during cell discharge, absent in long term storage under submersion as seen in Figure 9b and c. The change in surface morphology coincides with previous publication of Si RedOX cells,<sup>[1,24,25]</sup> and further emphasize that Si electro dissolution occurs during the discharge process.

Furthermore, the long-term storage at open air laboratory conditions at  $22 \pm 1^\circ\text{C}$  is displayed in Figure 9c. shows the minimal corrosive nature of the electrolyte on the Silicon wafer compared to active anodic polarization conditions and therefore tolerable. These results coincide with the computational modeling showing that there are no free water molecules in the electrolyte in the present stoichiometric ratio of water to Fluoride (3:1), enabling Fluoride bridging by water to form oligo-fluorinated species instead of forming solvation shells and free water that will undoubtedly contribute to parasitic corrosion of the Silicon as previously reported.<sup>[56]</sup>

Both solute analysis and Si wafer etching further emphasize the oxidation of Si to yield the most plausible full-cell reactions accordingly:



### Mechanical charging

With profound insight regarding cell operation and termination mechanism, mechanical charging was examined as an alternative means of charging, due to the overwhelmingly higher Si wafer capacity of 885 mAh in an exposed area of  $\text{cm}^2$  vs. the cathode with a theoretical capacity of 13.2 mAh at the current cell configuration. Thus, it is feasible to mechanically replace

**Table 4.** Inductive Coupled Plasma (ICP) analysis of the full cell electrolyte at varied D.O.Ds.

Cell type	Depth of discharge (D.O.D)	Total S [mM]	Total Si [mM]
Si-Sulfur	0%	$0.1 \pm 0.06$	$0.4 \pm 0.1$
	50%	$10 \pm 2.1$	$22 \pm 2.6$
	100%	$28 \pm 5.3$	$58 \pm 6.5$
Si- $\text{FeF}_3$	0%	$0.9 \pm 0.03$	$0.6 \pm 0.1$
	50%	$21 \pm 2.8$	$12 \pm 1.9$
	100%	$138 \pm 15.5$	$47 \pm 4.8$
Si- $\text{CuF}_2$	0%	$0.1 \pm 0.04$	$0.9 \pm 0.2$
	50%	$1.2 \pm 0.10$	$31 \pm 0.9$
	100%	$1.6 \pm 0.09$	$7.6$

\* D.O.D assessed via the capacity obtained once the cells were operational terminated.

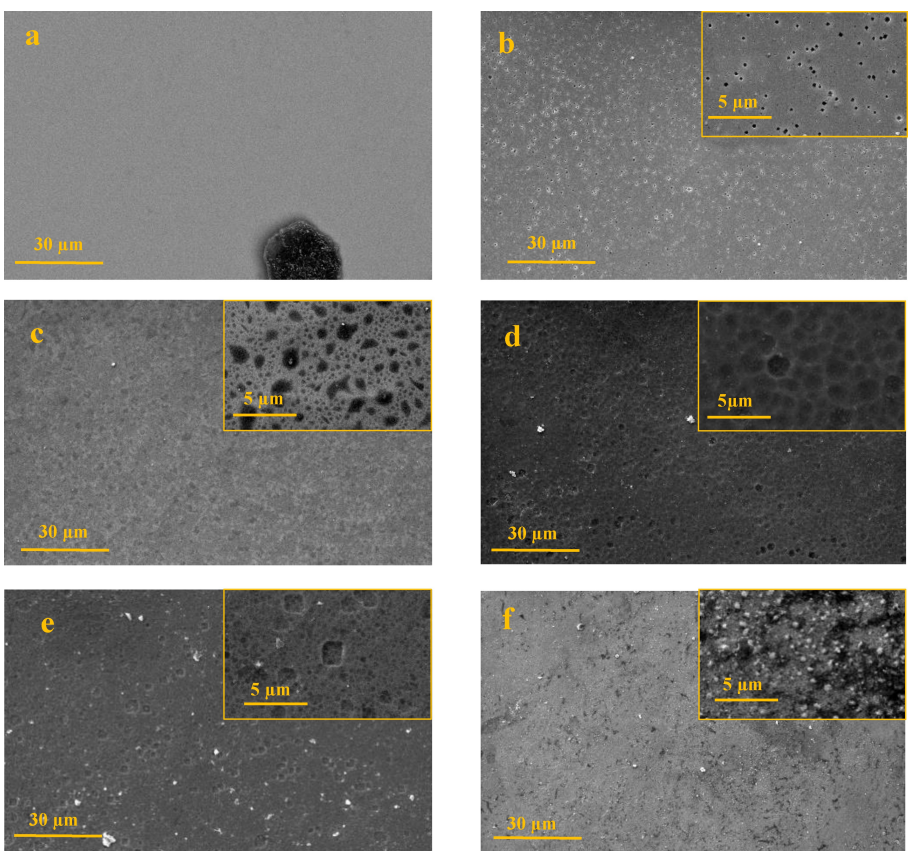


**Figure 9.** Scanning electron microscopy micrographs of: **a.** Pristine polished  $\text{Si}_{n++}$  wafer with a marker insignia for focus; **b.**  $\text{Si}_{n++}$  wafer submerged for nine months in a PC/EC 1:1 v/v% with 1.5[M] TBAF·3H<sub>2</sub>O electrolyte in an inert glovebox environment; **c.**  $\text{Si}_{n++}$  wafer submerged for 9 months in ambient atmosphere; **d.**  $\text{Si}_{n++}$  wafer after galvanostatic discharge against CuF<sub>2</sub> cathode; **e.**  $\text{Si}_{n++}$  wafer after galvanostatic discharge against S cathode; **f.**  $\text{Si}_{n++}$  wafer after galvanostatic discharge against FeF<sub>3</sub> cathode.

the cathode and the electrolyte until complete Si utilization. Failing cells were disassembled and the cathode was replaced in order to verify continuous cell functionality and examine the maximal capacity that can be obtained from the  $\text{Si}_{n++}$  wafer. The galvanostatic experiments are displayed in Figure 10a and exhibit prolonged anode functionality up to 35% of the theoretical anode capacity with approximately 30 consecutive cathode replacement. When the cells failed at below 80% cathode capacity, coinciding with every third cycle as indicated in Figure 10b the electrolyte was replaced to further stretch the limits of the anode. As can be observed from both figures, the capacity is maintained and there is a drastic fall every third cycle, coinciding with electrolyte replacement. At the end of the experimental runs the cells failed only as a result of leakage as the wafer was gradually etched and could no longer be sealed by the sealing rings, indicating mechanical and not electrochemical failure. Exact capacity obtained in each specific cycle is elaborated in the supplementary section **Table S19**.

The electrolyte was examined in every cell that failed below 80% cathode utilization in an array of identically constructed cells to shed further light on the discharge mechanism *via* ICP and IC for Si and F solutes respectively, the results in Figure 10c indicate consumption of fluorides during the Si oxidative dissolution process. This result implies oligo-fluoride species

degradation and depletion during the Si oxidative dissolution process, further emphasizing the importance of fluoride ions and their resulting speciation in the dissolution process along with the necessary concentration for proper cell operation above 800 (mM). Furthermore, the presence of Si in the electrolyte reinforces the mechanism of oxidative anode dissolution as well as the etched surface area portrayed in a typically etched  $\text{Si}_{n++}$  wafer in Figure 10d.

## Conclusions

This research lays forth a novel synergistic and rigorous design, model and analysis of a Si RedOx battery and its constituents. Physical electrolyte and solute characterization provided a critical information for quantum-mechanical DFT modeling, that concluded and predicted <sup>19</sup>F NMR shifts, solvation mechanisms and supramolecular chemical environments to yield the optimal solvent and solute concentration for fluoro-hydrogenate electrolytes. Molecular dynamics modeling concluded the optimal water to fluoride molar ratio to minimize electrolyte degradation and maximize more favorable characteristics as ionic conductivity and electroactive species. The complementary computational and experimental methodology enabled both

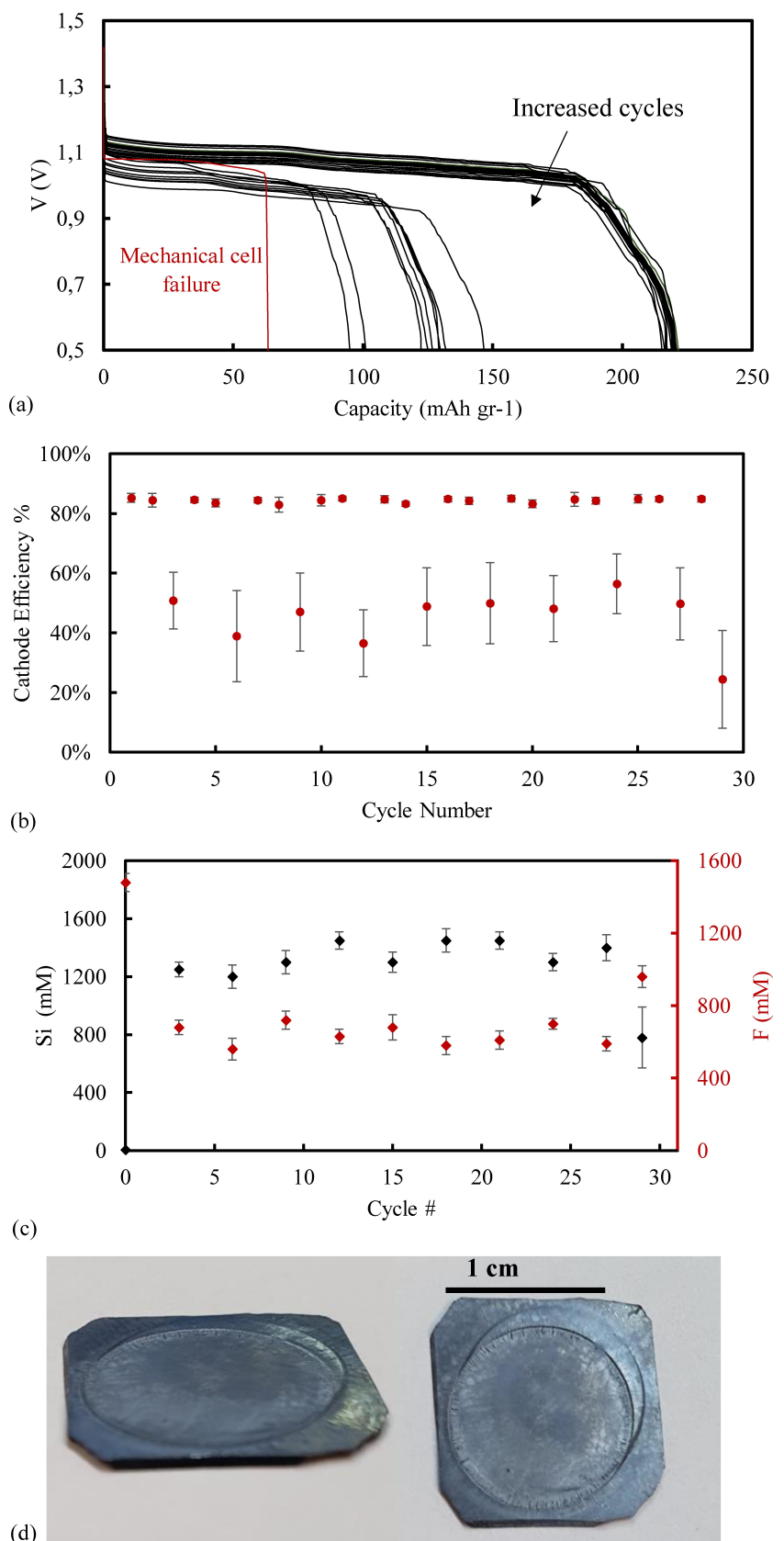


**Figure 10.** a. Mechanical charging via cathode and electrolyte replacement with the same  $\text{Si}_{n+}$  wafer anode with cathode efficiency calculated at the end of each cycle compared to the theoretical value, each cycle ran down to 0.5 [V] at a current density of 0.1 [ $\text{mA cm}^{-2}$ ]; b. cathode efficiency per cycle upon mechanical replacement until cell operational termination; c. analysis of soluble Si and F in the electrolyte (for every third mid cycle); d. top and side views of  $\text{Si}_{n+}$  wafer upon cell operational termination.

efficient Si anode surface activation, sufficient employed current densities and mitigation of the adverse effects of parasitic corrosion arising from soluble water. The optimal electrolyte, consisting of a mixture of PC/EC 1:1 v/v% with 1.5[M] of TBAF·3H<sub>2</sub>O, was assessed via full cell characterization with compatible cathode materials to reach up to 80% CE. Cell analysis showed both cathode reactivity and compatibility, Si anodic dissolution and electrolyte stability. Cell operational termination can be attributed to cathode degradation as the limiting factor, showcasing resilient and robust performance of the active Si anode that could be mechanically recharged up to 35% Si anode utilization, with mechanical cell leakage being the limiting factor. Altogether, a very optimistic outlook can be deduced from this body of work, as it pertains to cell customization, design via predictive modeling, cell operation and characterization towards the next generation of Si anode-based batteries.

## Experimental section

### Cell assembly

All cell parts were kept and assembled at ambient laboratory atmosphere 22±1°C. Heavy doped Si wafers [Si<sub>n++</sub>] n-type 422 orientation <100>, Arsenic doped, 0.001–0.005 (Ω·cm) 500±25 (μm) thickness, washed with Acetonitrile (Sigma Aldrich, 99.8%), wiped and dried under a Nitrogen stream. Platinum foil (Good-Fellow 99.999%) was submerged in aqua regia for 1–2 minutes and washed with DIW and dried under a Nitrogen stream. Cells were assembled in accordance with a previous publication.<sup>[1]</sup> and left to rest for 3 hours prior to each experiment to test for leaks. After each experiment, the cells were disassembled and checked for leaks and rinsed with Acetonitrile and left to dry in an ambient atmosphere.

### Material preparation

All powder materials were dried in a vacuum oven at 110°C for 24 hours prior to weighing. Cathode slurries were prepared with a ratio of 10%w/w conductive carbon (CB) additive (40%w/w for the Sulfur based slurry to improve conductivity), 10%w/w of binding polymer-Polyvinylidene-di-fluoride (PVDF) and the rest was the active cathode material. The slurries were mixed in borosilicate glass vials with N-methyl pyrrolidone (NMP) as the solvent. The slurries were left to stir for 24 hours prior to application on an Aluminum foil via Doctor Blade and dried in a vacuum oven at 110°C for 3 hours. All solvents were tested in a Karl Fischer coulometric titrator and contained under 25 ppm of water. Potassium fluoride salts were dried in a vacuum oven at 200°C for 48 hours prior to weighing and TBAF·3H<sub>2</sub>O by Sigma-Aldrich® was used as received.

### Nuclear magnetic resonance (NMR) spectroscopy

NMR spectra were obtained using Inova 500 spectrometer. All samples were diluted at a 1:1 ratio with CDCl<sub>3</sub> for signal locking. Chemical shifts for Fluorine (<sup>19</sup>F) are reported in parts per million and are referenced to Hexafluoro Benzene ( $\delta$ =−164.9 ppm) which was added in trace amounts to each sample.

### Fourier transform infra-red spectroscopy

Fourier transform infrared Spectroscopy with attenuated total reflection (FTIR-ATR) was used by performing 64 scans with data spacing of 0.241 (cm<sup>−1</sup>). The measurements were performed utilizing a Thermo Fisher Nicolet IS5 spectrometer equipped with an additional diamond crystal with an incident angle of 45° ATR.

### Solute analysis

Electrolytes were analyzed via Ion Chromatography IC (930 compact IC flex) for fluoride concentration and Inductively Coupled Plasma ICP (iCAP PRO Series ICP-OES) for dissolved Si, and other elements. All electrolytes were diluted with DDIW at a ratio of 40:1 v/v%.

### Electrochemical measurements

Ionic conductivity was measured via a conductivity meter (Consort multiparameter analyzer C3030 using SK23T consort electrode) with a cell constant of 10 [cm<sup>−1</sup>]. Instrument calibration was performed using 0.01[M], 0.1[M], 1[M] and 5[M] aqueous KCl calibration solutions. Temperature range 22±1°C. Open Circuit potential (OCP) measurements were carried out using a Biologic VSP Potentiostant/Galvanostat in a two-cell configuration with Fc/Fc+ on a Pt wire as a reference electrode. Half-cell Electrochemical Impedance Spectroscopy (EIS) and Potentiodynamic experiments were carried out via a three-electrode configuration with Pt foil as a counter electrode and Fc/Fc+ on a Pt wire as a reference electrode. Exposed foil dimensions 1×1 (cm<sup>2</sup>) and a 0.8 (cm) distance between electrodes. The cells' active area was isolated via nitrile rubber sealing O-rings. Electrolyte volume was constant in all cells at 0.5 (ml). EIS Measurements were acquired between 100 mHz and 100 KHz with an amplitude of 10 mV.

### Cathode characterization

Cathode phase characterization was conducted using an XRD analyzer: MiniFlex Rigaku, Japan, with Cu<sub>κα</sub> radiation  $\lambda$ =1.54178 Å and a Graphite monochromator, scan angles from 15° to 80° with a 0.1°/min scan speed.

### Surface Characterization

Phenom XL G2 Desktop SEM was utilized for the Si<sub>n++</sub> wafers and cathode surface morphology and elemental composition analysis via Electron Dispersive Spectroscopy (EDS). All specimens were rinsed with Isopropyl alcohol and dried under a Nitrogen stream prior to analysis.

### Quantum-chemical modeling

Quantum-chemical modeling of Fluorine-containing species in the gas phase (vacuum) and different solvents was performed using the density functional theory (DFT) implemented in the Gaussian16 software.<sup>[57]</sup> The Austin-Frisch-Petersson hybrid functional with dispersion (APFD)<sup>[58]</sup> with the 6-311+G(2d,p) basis set was used for this purpose. A full geometry optimization followed by vibration calculation for the minimum on the potential energy surface was performed for each species. The effect of solvation was examined using two types of continuum approaches: Solvation Model based on Density (SMD) and Integral Equation Formalism Polarizable Continuum Model (IEPCM). The SMD model<sup>[59]</sup> is based on solute electron density and on a continuum model of the solvent defined

by the bulk dielectric constant and atomic surface tensions. It belongs to the family of Self-Consistent Reaction Field (SCRF) methods<sup>[60]</sup> in which, the solvent is treated as a continuous and uniform dielectric medium characterized by its dielectric constant  $\epsilon$ . The solute is placed inside a cavity within the solvent medium, while the interaction between the solute and the solvent is treated as a mutual polarization caused by electrostatic forces. The SMD method was parametrized using a large training set consisting of 2821 solute-solvent pairs, including ions.<sup>[59]</sup> The SMD method can be applied to predict the solvation free energy of any charged or uncharged solute in any solvent using the calculated electronic structure of the solute and the following macroscopic solvent parameters: dielectric constant ( $\epsilon$ ), the square of the refractive index ( $n^2$ ), macroscopic surface tension ( $\gamma$ ), Abraham-type hydrogen-bond acidity and basicity parameters ( $\sum \alpha_2^H$  and  $\sum \beta_2^H$ ), the fraction of aromatic carbon atoms ( $\phi$ ), and the fraction of electronegative halogen atoms ( $\psi$ ). All parameters are elaborated in the supplementary section **Table S1**.

Like SMD, the IEFPCM (Integral Equation Formalism for Polarizable Continuum Models) method<sup>[61]</sup> also belongs to the family of SCRF methods. Although IEFPCM reproduces in typical cases the experimental values of solvation free energy less accurately than SMD due to the use of a large training set of experimental data for the parameterization of the latter, the benefits of SMD may be lost in the application of compounds belonging to chemical classes poorly represented in the training set, especially inorganic ions. In the latter case, when predicting the free energy of solvation, it is recommended to combine the use of SMD and other continuum methods with cluster-pair approximation, which implies quantum-chemical modeling of solute-solvent clusters.<sup>[59,62]</sup> Moreover, IEFPCM enables focus only on the consideration of the effect of electrostatic polarization on solvation. Since within the framework of the IEFPCM method only one parameter, the dielectric constant, is used to describe the solvent, the use of this method makes it possible to consider smooth functional dependences of solvation-dependent properties on a single argument that has a clear physical meaning.

When predicting NMR spectra,  $^{19}\text{F}$  shielding was calculated at the APFD/6-311+G(2d,p) theory level using the GIAO method,<sup>[63,64]</sup> and the corresponding chemical shifts were assessed using the calculated value +168.08 ppm for  $\text{CFCl}_3$  as a reference.

Atomistic molecular dynamics (MD) studies were performed using the LAMMPS program.<sup>[65]</sup> Input files for simulations were prepared using the Moltemplate tool<sup>[66]</sup> by assembling templates based on the GROMOS 54 A7 force field,<sup>[67]</sup> for electrolyte components retrieved from the ATB repository.<sup>[68,69]</sup> The ATB template codes used for this purpose are: PK42 for TBA cations, L5VB for fluoride anions, 49E1 for water molecules, 1N41 for EC molecules, and VQC for PC molecules. The initial simulation box was built by packing the molecules of all electrolyte components using the PACKMOL software.<sup>[70,71]</sup> Simulations were run for 2 ns under the NPT settings (isothermal-isobaric ensemble) at a temperature of 300 K and a pressure of 1 atmosphere. The obtained MD trajectories were visualized using the VMD software<sup>[72]</sup> and analyzed using the PyLAT tool.<sup>[73]</sup> Distributions of interatomic distances were analyzed using the CrystalMaker program.<sup>[74]</sup>

## Supporting Information

Supporting Information is available from the Wiley Online Library or from the author.

## Acknowledgements

The authors acknowledge the financial support of the Israeli Ministry of Aliyah and Integration, supporting I.B. through the Center for Integration in Science, and the infrastructure support provided by the Grand Technion Energy Program (GTEP) and the Israel National Institute for Energy Storage (INIES).

## Conflict of Interests

The authors declare that they have no known competing financial interests or personal relationships that could have appeared to influence the work reported in this paper.

## Data Availability Statement

The data that support the findings of this study are available from the corresponding author upon reasonable request.

**Keywords:** Si-based batteries · non aqueous solvents · fluoride electrolyte · cathode materials · computational studies

- [1] A. Epshtain, I. Baskin, M. Suss, Y. Ein-Eli, *Adv. Energy Mater.* **2022**, *12*, DOI: 10.1002/AENM.202201626.
- [2] I. Baskin, A. Epshtain, Y. Ein-Eli, *J. Mol. Liq.* **2022**, *351*, DOI: 10.1016/j.molliq.2022.118616.
- [3] A. Chew, N. A. Polytechnic, **2023**, DOI: 10.13140/RG.2.2.23347.40481.
- [4] M. Nizam, H. Maghfiroh, A. Ubaidilah, I. Inayati, F. Adriyanto, *Int. J. Power Electron. Drive Syst.* **2022**, *13*, 926–937.
- [5] Y. E. Durmus, H. Zhang, F. Baakes, G. Desmaizieres, H. Hayun, L. Yang, M. Kolek, V. Küpers, J. Janek, D. Mandler, S. Passerini, Y. Ein-Eli, *Adv. Energy Mater.* **2020**, *10*, DOI: 10.1002/aenm.202000089.
- [6] E. Phiddian, "How zinc batteries could power the sustainable economy" can be found under <https://cosmosmagazine.com/technology/zinc-batteries-improvements-needed/>, **2022**.
- [7] J. Ming, J. Guo, C. Xia, W. Wang, H. N. Alshareef, *Mater. Sci. Eng. R* **2019**, *135*, 58–84.
- [8] N. Zhang, X. Chen, M. Yu, Z. Niu, F. Cheng, J. Chen, *Chem. Soc. Rev.* **2020**, *49*, 4203–4219.
- [9] P. He, Q. Chen, M. Yan, X. Xu, L. Zhou, L. Mai, C. W. Nan, *EnergyChem* **2019**, *1*, DOI: 10.1016/j.enchem.2019.100022.
- [10] R. D. McKerracher, C. Poncedeleon, R. G. A. Wills, A. A. Shah, F. C. Walsh, *ChemPlusChem* **2015**, *80*, 323–335.
- [11] H. A. Figueroa-Rodríguez, R. D. McKerracher, M. Insausti, A. G. Luis, C. P. de León, C. Alegre, V. Baglio, A. S. Aricó, F. C. Walsh, *J. Electrochem. Soc.* **2017**, *164*, A1148–A1157.
- [12] C. Wang, Y. Yu, J. Niu, Y. Liu, D. Bridges, X. Liu, J. Pooran, Y. Zhang, A. Hu, *Appl. Sci.* **2019**, 1–22,
- [13] E. T. Sayed, A. J. O. Al Marzooqi, M. A. Abdelkareem, A. G. Olabi, *Encycl. Smart Mater.* **2021**, *2*, 115–124.
- [14] S. Kundu, N. Solomatin, A. Kravtsev, Y. Ein-Eli, *Energy Technol.* **2022**, *10*, DOI: 10.1002/ente.202200896.
- [15] R. Shah, V. Mittal, E. Matsil, A. Rosenkranz, *Adv. Mech. Eng.* **2021**, *13*, 1–9.
- [16] R. Mohtadi, F. Mizuno, *Beilstein J. Nanotechnol.* **2014**, *5*, 1291–1311.
- [17] N. R. Levy, S. Lifshits, E. Yohanan, Y. Ein-Eli, *ACS Appl. Energ. Mater.* **2020**, *3*, 2585–2592.
- [18] N. R. Levy, M. Auinat, Y. Ein-Eli, *Energy Storage Mater.* **2018**, *15*, 465–474.
- [19] I. D. Hosein, *ACS Energy Lett.* **2021**, *6*, 1560–1565.
- [20] T. Ouchi, H. Kim, X. Ning, D. R. Sadoway, *J. Electrochem. Soc.* **2014**, *161*, A1898–A1904.
- [21] T. Ouchi, H. Kim, B. L. Spatocco, D. R. Sadoway, *Nat. Commun.* **2016**, *7*, 1–5.
- [22] H. Kim, D. A. Boysen, T. Ouchi, D. R. Sadoway, *J. Power Sources* **2013**, *241*, 239–248.

- [23] R. Bansal, P. Menon, *SN Appl. Sci.* **2020**, *2*, 1–17.
- [24] G. Cohn, R. A. Eichel, Y. Ein-Eli, *Phys. Chem. Chem. Phys.* **2013**, *15*, 3256.
- [25] G. Cohn, A. Altberg, D. Macdonald, Y. Ein-Eli, *Electrochim. Acta* **2011**, *58*, 161–164.
- [26] G. Cohn, Y. Ein-Eli, *J. Power Sources* **2010**, *195*, 4963–4970.
- [27] R. Hagiwara, T. Hirashige, T. Tsuda, Y. Ito, *J. Electrochem. Soc.* **2002**, *149*, D1.
- [28] L. Zhou, S. Tian, X. Du, T. Liu, H. Zhang, J. Zhang, S. Hu, Z. Chen, J. Zhang, G. Cui, *ACS Energy Lett.* **2023**, *8*, 40–47.
- [29] B. S. Jayathilake, E. J. Plichta, M. A. Hendrickson, S. R. Narayanan, *J. Electrochem. Soc.* **2018**, *165*, A1630–A1638.
- [30] N. M. Do, M. A. Olivier, J. J. Salisbury, C. B. Wager, *Anal. Chem.* **2011**, *83*, 8766–8771.
- [31] H. Sun, S. G. DiMaggio, *J. Am. Chem. Soc.* **2005**, *127*, 2050–2051.
- [32] R. K. Sharma, J. L. Fry, *J. Org. Chem.* **1983**, *48*, 2112–2114.
- [33] D. Phillip Cox, J. Terpinski, W. Lawrynowicz, *J. Org. Chem.* **1984**, *49*, 3216–3219.
- [34] N. Gommermann, P. Knochel, *Org. Synth.* **2007**, *84*, 1, DOI: 10.15227/orgsyn.084.0001
- [35] G. Pe, L. Gonza, *J. Phys. Chem. A* **2012**, DOI: 10.1021/jp3058383
- [36] K. Matsumoto, R. Hagiwara, *Fluorohydrogenate Ionic Liquids, Liquid Crystals, and Plastic Crystals*, Elsevier, **2015**.
- [37] Y. Saito, K. Hirai, K. Matsumoto, R. Hagiwara, Y. Minamizaki, *J. Phys. Chem. B* **2005**, *109*, 2942–2948.
- [38] R. Hagiwara, Y. Nakamori, K. Matsumoto, Y. Ito, *J. Phys. Chem. B* **2005**, *109*, 5445–5449.
- [39] L. Y. Beaulieu, J. R. Dahn, *J. Electrochem. Soc.* **2018**, DOI: 10.1149/2.0981803jes
- [40] M. S. Ding, *J. Electrochem. Soc.* **2003**, *150*, A455.
- [41] C. Wohlfarth, in *Landolt-Börnstein IV/24: Surface Tension of Pure Liquids and Binary Liquid Mixtures* (Ed.: M.D. Lechner), Springer US, New York, NY, **2008**, *34*, 77–77, DOI: 10.1007/978-3-540-75508-1\_42
- [42] R. K. Sharma, F. L. James, *Chem. Rev.* **1980**, *80*, 2112–2114.
- [43] V. K. Davis, S. Munoz, J. Kim, C. M. Bates, N. Momčilović, K. J. Billings, T. F. Miller, R. H. Grubbs, S. C. Jones, *Mater. Chem. Front.* **2019**, *3*, 2721–2727.
- [44] H. Nakano, T. Matsunaga, T. Mori, K. Nakanishi, Y. Morita, K. Ide, K. I. Okazaki, Y. Orikasa, T. Minato, K. Yamamoto, Z. Ogumi, Y. Uchimoto, *Chem. Mater.* **2021**, *33*, 459–466.
- [45] B. S. Ault, *J. Phys. Chem.* **1979**, *83*, 837–844.
- [46] R. Hagiwara, Y. Nakamori, K. Matsumoto, Y. Ito, *J. Phys. Chem. B* **2005**, *109*, 5445–5449.
- [47] T. Enomoto, Y. Nakamori, K. Matsumoto, R. Hagiwara, *J. Phys. Chem. C* **2011**, *115*, 4324–4332.
- [48] M. Gerken, J. A. Boatz, A. Kornath, R. Haiges, S. Schneider, T. Schroer, K. O. Christe, *J. Fluorine Chem.* **2002**, *116*, 49–58.
- [49] K. Matsumoto, R. Hagiwara, *Ionic Liquid Materials Based on Fluoroanions*, Elsevier Inc., **2017**.
- [50] C. L. Liotta, H. P. Harris, *J. Am. Chem. Soc.* **1974**, *96*, 2250–2252.
- [51] R. Schwesinger, R. Link, P. Wenzl, S. Kossek, *Chem. A Eur. J.* **2005**, *12*, 438–445.
- [52] T. Borrmann, E. Lork, R. Mews, W. D. Stohrer, *J. Fluorine Chem.* **2004**, *125*, 903–916.
- [53] X. Hua, R. Robert, L. Du, K. M. Wiaderek, M. Leskes, K. W. Chapman, P. J. Chupas, C. P. Grey, *J. Phys. Chem. C* **2014**, *118*, 15169–15184.
- [54] W. Ren, W. Ma, S. Zhang, B. Tang, *Energy Storage Mater.* **2019**, *23*, 707–732.
- [55] G. Di Donato, T. Ates, H. Adenusi, A. Varzi, M. A. Navarra, S. Passerini, *Batteries & Supercaps* **2022**, *5*, DOI: 10.1002/batt.202200097.
- [56] G. Cohn, D. D. MacDonald, Y. Ein-Eli, *ChemSusChem* **2011**, *4*, 1124–1129.
- [57] M. J. Frisch, G. W. Trucks, et al., *Gaussian 16, Revision C.01*, **2016**, Gaussian, Inc., Wallin.
- [58] A. Austin, G. A. Petersson, M. J. Frisch, F. J. Dobek, G. Scalmani, K. Throssell, *J. Chem. Theory Comput.* **2012**, *8*, 4989–5007.
- [59] A. V. Marenich, C. J. Cramer, D. G. Truhlar, *J. Phys. Chem. B* **2009**, *113*, 6378–6396.
- [60] J. Tomasi, B. Mennucci, R. Cammi, *Chem. Rev.* **2005**, *105*, 2999–3093.
- [61] E. Cancès, B. Mennucci, J. Tomasi, *J. Chem. Phys.* **1997**, *107*, 3032–3041.
- [62] C. P. Kelly, C. J. Cramer, D. G. Truhlar, *J. Phys. Chem. B* **2007**, *111*, 408–422.
- [63] J. Gauss, *Chem. Phys. Lett.* **1992**, *191*, 614–620.
- [64] J. Gauss, *Ber. Bunsen-Ges.* **1995**, *99*, 1001–1008.
- [65] A. P. Thompson, H. M. Aktulga, R. Berger, D. S. Bolintineanu, W. M. Brown, P. S. Crozier, P. J. in't Veld, A. Kohlmeyer, S. G. Moore, T. D. Nguyen, R. Shan, M. J. Stevens, J. Tranchida, C. Trott, S. J. Plimpton, *Comp. Phys. Commun.* **2022**, *271*, 108171.
- [66] A. I. Jewett, D. Stelter, J. Lambert, S. M. Saladi, O. M. Roscioni, M. Ricci, L. Autin, M. Maritan, S. M. Bashusqeh, T. Keyes, R. T. Dame, J.-E. Shea, G. J. Jensen, D. S. Goodsell, *J. Mol. Biol.* **2021**, *433*, 166841.
- [67] N. Schmid, A. P. Eichenberger, A. Choutko, S. Riniker, M. Winger, A. E. Mark, W. F. Van Gunsteren, *Eur. Biophys. J.* **2011**, *40*, 843–856.
- [68] A. K. Malde, L. Zuo, M. Breeze, M. Stroet, D. Pogar, P. C. Nair, C. Oostenbrink, A. E. Mark, *J. Chem. Theory Comput.* **2011**, *7*, 4026–4037.
- [69] M. Stroet, B. Caron, K. M. Visscher, D. P. Geerke, A. K. Malde, A. E. Mark, *J. Chem. Theory Comput.* **2018**, *14*, 5834–5845.
- [70] J. M. Martínez, L. Martínez, *J. Comput. Chem.* **2003**, *24*, 819–825.
- [71] L. Martínez, R. Andrade, E. G. Birgin, J. M. Martínez, *J. Comput. Chem.* **2009**, *30*, 2157–2164.
- [72] W. Humphrey, A. Dalke, K. Schulten, *J. Mol. Graphics* **1996**, *14*, 33–38.
- [73] M. T. Humbert, Y. Zhang, E. J. Maginn, *J. Chem. Inf. Model.* **2019**, *59*, 1301–1305.
- [74] D. C. Palmer, *Crystal maker program*. Oxfordshire, United Kingdom **2014**.

Manuscript received: December 5, 2023

Revised manuscript received: December 10, 2023

Accepted manuscript online: December 11, 2023

Version of record online: January 6, 2024